Artificial Intelligence-Based Adaptive Control of a Liquid Resistance Starter for a 5 MW Slip-Ring Induction Motor in Oil and Gas Installations

Muralidharan Dhandapani[1], Soumyakant Satapathy[2]

[1,2]Electrical and Electronics Engineering, Technical and Administrative Training Institute (TATI), Muscat, Oman

Abstract
High-power slip-ring induction motors remain important in oil and gas installations where high breakaway torque, restricted network capacity and severe operating conditions complicate starting. Conventional liquid resistance starters (LRSs) generally follow a predetermined electrode-travel schedule and therefore cannot compensate explicitly for changing load torque, electrolyte conductivity or actuator constraints. This study develops an adaptive starting framework combining a quadratic B-spline neural disturbance estimator, a bounded sliding-mode-inspired correction, constrained rotor-resistance selection and a physically consistent electrode/thermal model. The framework is assessed using an original, deterministic reduced-order numerical simulation of a 5 MW, 6.6 kV, four-pole wound-rotor motor; it is not presented as a laboratory experiment, plant trial or MATLAB/Simulink electromagnetic-transient model. For a combined scenario with 30% conductivity degradation, elevated ambient temperature, load changes and oscillatory disturbance, the adaptive controller decreases integral absolute error from 6.398 to 5.553 pu·s (13.2%), integral squared error by 20.7%, and the time to 95% synchronous speed from 33.46 to 30.70 s. Peak current remains essentially unchanged at 1.501 pu, while predicted LRS energy increases from 56.98 to 57.98 MJ. The findings therefore support improved speed tracking and faster acceleration, while identifying a modest thermal-energy trade-off that requires explicit design attention.

Keywords: liquid resistance starter; slip-ring induction motor; wound-rotor motor; B-spline neural network; adaptive control; sliding-mode control; motor starting; oil and gas.

1. Introduction

Large pumps, compressors, mills, crushers and process conveyors can impose high starting torque, substantial reflected inertia and strict limits on voltage depression. In established petroleum and process facilities, wound-rotor induction motors remain attractive where an accessible rotor circuit allows starting torque and current to be shaped by external resistance. An LRS inserts an electrolytic resistance into the three rotor phases and progressively lowers that resistance as speed increases. Commercial equipment commonly contains three fixed and three moving electrodes, an electrode-drive motor, an agitator, a control cubicle and a rotor short-circuit contactor [1, 2].

The effectiveness of this approach depends on the actual electrical resistance presented by the electrolyte, rather than simply on the elapsed time after a start command. Conductivity changes with temperature, solution concentration, contamination and ageing, while the torque demanded by the driven equipment depends on process conditions. A timer-only electrode trajectory can consequently be satisfactory at commissioning yet become poorly matched to subsequent starts. In weak industrial networks, the consequences can include longer acceleration, greater bus-voltage depression, elevated starter temperature and avoidable mechanical stress [3, 4].

Artificial-intelligence-assisted control provides a practical route to estimating operating uncertainty from measured speed, current and actuator position. Beltran-Carbajal et al. demonstrated B-spline artificial neural networks for robust induction-motor control, while Tapia-Olvera et al. examined adaptive B-spline-based regulation of induction-motor position [5, 6]. Those studies establish the relevance of locally supported neural approximators, but they do not by themselves constitute evidence that an LRS electrode actuator, electrolyte model or motor-starting constraint has been validated.

The present contribution is therefore defined narrowly: it adapts the B-spline disturbance-estimation idea to an explicitly modelled liquid-rotor-resistance starting system, adds a constrained electrode-position selection stage, includes conductivity/temperature coupling and evaluates three reproducible numerical operating scenarios. All figures and numerical results reported here were generated specifically for the present reduced-order model; previously published performance tables and illustrations are not reused.

The central research question is whether online disturbance estimation and bounded resistance selection improve speed-reference tracking and acceleration under realistic starter constraints, and whether those improvements necessarily reduce peak current or starter thermal burden. The latter distinction is essential because a controller that improves one objective can worsen another.

2. Literature Review and Research Gap

2.1 Liquid resistance starting and industrial practice

A wound-rotor induction machine exposes its rotor windings through slip rings, enabling external resistance to be inserted during acceleration. Manufacturer documentation identifies the main elements of a high-power electrolytic starter as segregated phase compartments, fixed and moving electrodes, a motorised positioning mechanism and a short-circuiting contactor [1, 2]. IEEE 3002.7 frames motor-starting studies in terms of the complete industrial power system, including available network strength, load acceleration and acceptable voltage performance, rather than motor current alone [3]. ABB documentation also identifies slip-ring motors as suitable where high starting torque and limited starting current are important [7].

A technically important clarification is that electrode immersion is not a universal proxy for resistance. Depending on the construction, the manipulated geometry may change electrode separation, conducting area or both. The resistance increases with effective current-path length and decreases as effective conducting area or electrolyte conductivity increases. Therefore, phrases such as 'fully immersed always means maximum resistance' are not generally valid; the actual direction must be established from the manufacturer's geometry and commissioning data [1].

2.2 Neural approximation and robust nonlinear control

B-spline basis functions provide local support: modifying one coefficient mainly changes the approximation in a limited input interval. This property supports bounded online learning and makes low-order networks attractive for embedded control. Beltran-Carbajal et al. integrated B-spline neural adaptation with robust induction-motor control and reported detailed trajectory-tracking studies [5]. Tapia-Olvera et al. investigated an adaptive B-spline regulation strategy for induction-motor position [6]. The mathematical basis and local-support characteristics are also documented in MIT's B-spline treatment [8]. Sliding-mode methods address bounded model uncertainty by driving a suitably defined tracking variable towards a prescribed surface. Their industrial application must account for actuator limits and chattering; replacing an ideal discontinuous sign function with a smooth saturation or hyperbolic tangent reduces excessive switching demand. Utkin's treatment of sliding modes and electric-drive applications provides the relevant theoretical foundation [9, 10]. In the present work the sliding-mode term is a bounded robustness component, not a claim that an ideal discontinuous controller has been implemented on industrial hardware.

2.3 Identified gap and stated contribution

Existing induction-motor neural-control studies primarily address electrical drive control, position or trajectory regulation. A liquid starter adds a slower electromechanical actuator, electrolyte-dependent resistance, explicit starter heating, bypass sequencing and independent plant-protection requirements. The original contribution of this paper is the integrated system-level formulation of those LRS-specific features and a newly generated, transparently identified numerical comparison. The work does not claim the invention of B-spline neural networks or sliding-mode control, and it does not substitute simulation for laboratory or field validation.

3. System Description and Physical Modelling

3.1 Electrical and mechanical configuration

The investigated plant comprises a 6.6 kV industrial supply, a 5 MW three-phase wound-rotor induction motor, a process load and a three-phase electrolytic rotor starter. The motor stator is energised from the plant bus, while the rotor windings connect through slip rings to the LRS compartments. A geared positioning drive changes the effective electrode geometry until a dedicated contactor can short-circuit the rotor safely near operating speed. Current transformers, a voltage measurement, a speed sensor, an electrolyte-temperature sensor and electrode-position feedback provide the proposed measurement set.

Figure 1. Original proposed plant architecture, showing the wound-rotor motor, liquid starter, electrode actuator, adaptive controller and independent protection.

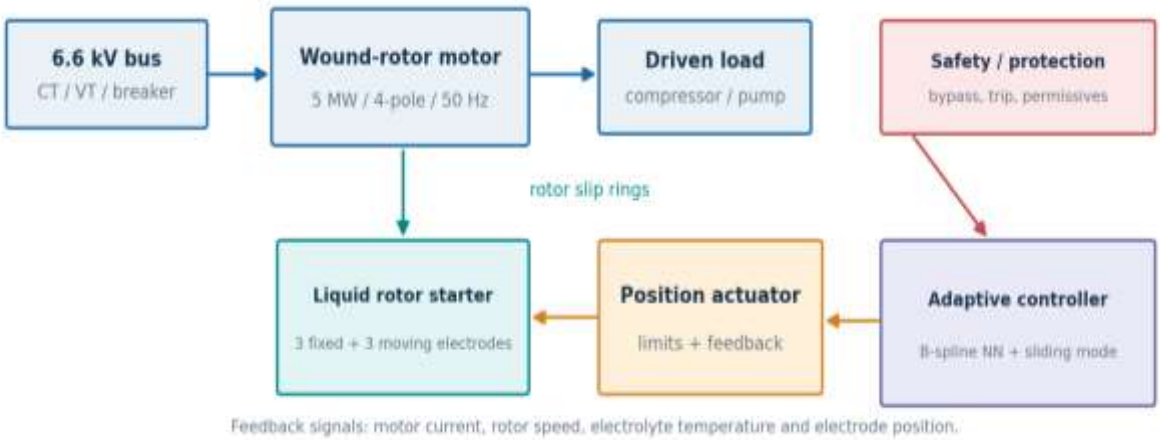

The supply, motor and protective functions must be treated as one coordinated installation. The adaptive algorithm is supervisory: it commands a permitted electrode position but does not override overcurrent protection, rotor short-circuit logic, travel limits, electrolyte level permissives, emergency stop functions or hazardous-area requirements [3, 4, 11].

3.2 Synchronous speed, slip and base quantities

$$n_s = \frac{120f}{p}, \qquad \omega_s = \frac{2\pi n_s}{60}, \qquad s = \frac{\omega_s - \omega_r}{\omega_s} \qquad (1)$$

$$T_\beta = \frac{P_r}{\omega_{r,rated}}, \qquad I_\beta = \frac{P_r}{\sqrt{3}\, VLL\eta \cos\varphi} \qquad (2)$$

For the selected 50 Hz, four-pole motor, synchronous speed is 1500 rpm and rated speed is 1470 rpm. The calculated rated torque and line-current bases are 32480.6 N·m and 517.3 A, respectively. All rotor-circuit parameters and plotted electrical quantities are referred consistently to the selected per-unit model. MathWorks notes that additional wound-rotor circuit parameters must be referred to the stator when connected to a stator-referred machine representation [12, 13].

3.3 Geometry- and temperature-dependent liquid resistance

$$R^{LRS}(\mathrm{x}, T, c) = \frac{\ell\mathrm{eff}}{[\sigma(\mathrm{T,C})\ \mathrm{Aeff(x)}]} \qquad (3)$$

$$\sigma(\mathrm{T, c}) = \sigma\mathrm{ref} \cdot \kappa\mathrm{c} \cdot [1 + \alpha\sigma(\mathrm{T} - \mathrm{Tref})] \qquad (4)$$

Here x denotes a normalised electrode-position command, ℓeff is effective current-path length, Aeff is effective conducting area, σ is electrolyte conductivity, κc is relative conductivity/concentration and ασ is an effective temperature coefficient. This first relationship is a geometry-informed lumped approximation; a real tank may require manufacturer-calibrated shape factors or finite-element field analysis.

$$R^{LRS}, \mathrm{pu} = \frac{\mathrm{R}_{min} + (\mathrm{R}_{max} - \mathrm{R}_{min})(1-\mathrm{x})^{1.45}}{\kappa\mathrm{c}[1 + \alpha\sigma(\mathrm{T} - \mathrm{Tref})]} \qquad (5)$$

The numerical case uses x = 0 for the maximum-resistance starter position and x = 1 for the minimum-resistance position. This is a coordinate convention, not a universal statement that all electrodes physically move upward or downward. The geometric exponent 1.45 is an explicit modelling assumption selected to represent a smooth nonlinear travel/resistance characteristic; it is not claimed to be a measured property of a particular commercial starter.

3.4 Reduced-order electromagnetic and mechanical equations

$$\mathrm{R\Sigma} = R_r' + R^{LRS} \qquad X_s = sX_{eq} \qquad (6)$$

$$T_e, \mathrm{pu} = \frac{\mathrm{KT} \cdot \mathrm{V}_{bus}^2 \cdot \mathrm{sR\Sigma}}{\mathrm{R\Sigma}^2 + (\mathrm{sX}_{eq})^2} \qquad (7)$$

$$\mathrm{I}_s, \mathrm{pu} = \sqrt{I_m^2 + [\mathrm{KI} \cdot \mathrm{sV}_{bus}/\sqrt{(\mathrm{R\Sigma}^2 + (\mathrm{sX}_{eq})^2)}]^2} \qquad (8)$$

$$\mathrm{V}_{bus}, \mathrm{pu} = \max\{\mathrm{V}_{min}, 1 - \mathrm{k}_{gridmax}(\mathrm{I}_s, \mathrm{pu} - 1{,}0)\} \qquad (9)$$

$$\mathrm{J}\,\frac{\mathrm{d}\omega_r}{dt} = \mathrm{T}_e - \mathrm{TL} - \mathrm{B}\omega_r \qquad (10)$$

Equations (6)–(8) are calibrated quasi-steady per-unit surrogates derived from the familiar resistance/slip dependence of induction-machine torque and current; they are deliberately identified as reduced-order relationships rather than a complete d–q electromagnetic-transient model. Stator flux dynamics, magnetic saturation, deep-bar effects, detailed source impedance angle and switching transients are not resolved. The voltage relationship is a scalar network-strength approximation and therefore cannot replace a formal plant motor-starting study under IEEE 3002.7 [3].

3.5 Electrode-actuator and thermal dynamics

$$\dot{\mathrm{x}} = \mathrm{sat}[(\mathrm{x}^* - \mathrm{x})/\tau_a, -\mathrm{V}_{max}, \mathrm{V}_{max}], \quad 0 \le x \le 1 \qquad (11)$$

$$\mathrm{C}_{th}\frac{\mathrm{dT}}{\mathrm{dt}} = \mathrm{P}_{LRS} - \mathrm{C}_{th}(\mathrm{T} - \mathrm{T}_{amb})/\tau_{cool} \qquad (12)$$

$$P_{LRS} \approx T_e \omega_s s \cdot R^{LRS} / (R'_r + R^{LRS}) \quad (13)$$

The actuator equation limits both total travel and electrode velocity. The electrolyte is represented by a single bulk-temperature state with effective thermal capacitance and a cooling time constant. The LRS loss expression approximates the external fraction of rotor slip power. It does not resolve local boiling, electrode current density, stratification, gas evolution or nonuniform tank temperature, so thermal conclusions must be interpreted only at screening-study level.

4. Proposed AI-Based Adaptive Control Framework

4.1 Supervisory control structure

The controller consists of an S-curve reference generator, a speed-error/sliding-surface calculation, a quadratic B-spline uncertainty estimator, a constrained rotor-resistance selector and a rate-limited electrode actuator. The manipulated variable is electrode position, not stator voltage or inverter switching state. This distinction connects the neural-control concept directly to the physical LRS mechanism.

Figure 2. Original adaptive-control signal path from speed reference to bounded electrode positioning, including online B-spline disturbance estimation.

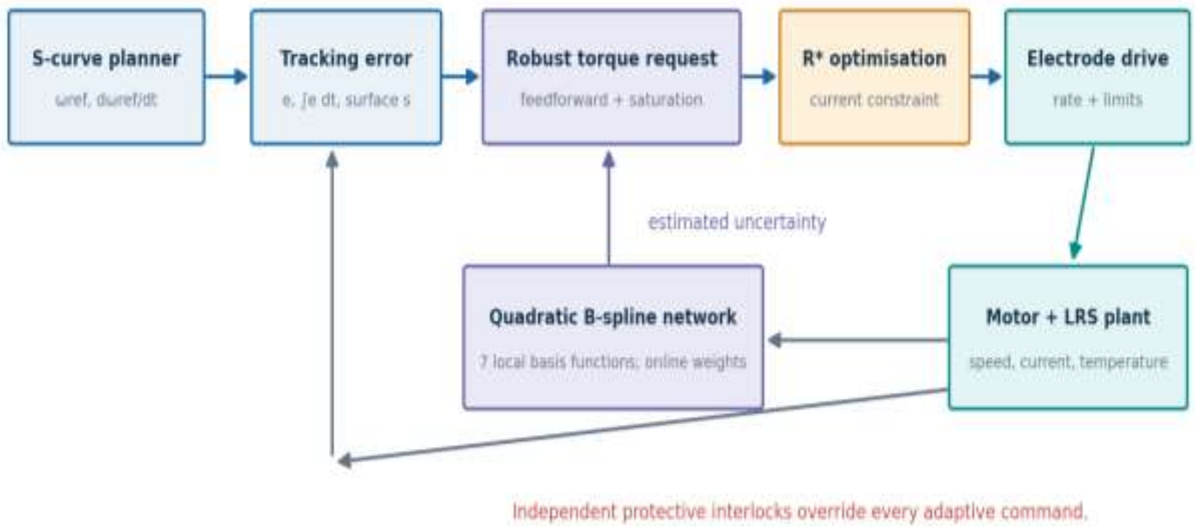

4.2 Starting reference and tracking surface

$$z = \min(t/t_r, 1),\ \omega_{ref}, \text{pu} = 0.985(3z^2 - 2z^3) \quad (14)$$

$$e = \omega_{ref}, \text{pu} - \omega_r, \text{pu}\ ,\ S = \lambda \int e\, dt \quad (15)$$

The cubic reference provides a smooth initial and final slope and defines a common comparison target for both controllers. The integral contribution reduces persistent offset, while anti-windup limits prevent a prolonged start or actuator saturation from creating an unbounded internal command. Because a fixed-frequency wound-rotor machine cannot arbitrarily control torque below the minimum achievable torque associated with the initial electrode position, exact early-time tracking is not expected.

4.3 Quadratic B-spline uncertainty estimator

$$\hat{d}(\omega_r) = \sum_{i=1}^{7} w_i B_i,\ \ 2(\omega_r) \quad (16)$$

$$B_i, 0(z) = 1 \text{ for } t_i \le z \le t_i + 1 \text{ otherwise } B_i, 0(z) = 0 \quad (17)$$

$B_i, p(z) = [(\mathrm{z} - \mathrm{t}_i)/(\mathrm{t}_i + \mathrm{p} - \mathrm{t}_i)]B_i, \mathrm{p} - 1(\mathrm{z}) + [(\mathrm{t}_i + \mathrm{p} + 1 - \mathrm{z})/(\mathrm{t}_i + \mathrm{p} + 1 - \mathrm{t}_i + 1)]\, B_i + 1, \mathrm{p} - 1(\mathrm{z})$ (18)

$\dot{\mathrm{w}}_i = \gamma \mathrm{B}_i, 2(\omega_\mathrm{r})[\mathrm{d}_{meas} - \hat{\mathrm{d}}] - \mu \mathrm{w}_i, \quad \mathrm{w}_{min} \leq \mathrm{w}_i \leq \mathrm{w}_{max}$ (19)

Seven quadratic basis functions are distributed across normalised motor speed using a clamped knot vector. Their local support means that a load-estimation error mainly modifies weights associated with the current speed region. The adaptation law uses learning rate γ = 0.24, leakage μ = 0.035 and bounded weights. These are model-specific parameters selected for the present numerical experiment; they are not copied from published B-spline controller tables.

Figure 3. Original quadratic B-spline basis functions and the 24 s smooth speed-reference trajectory used in the numerical study.

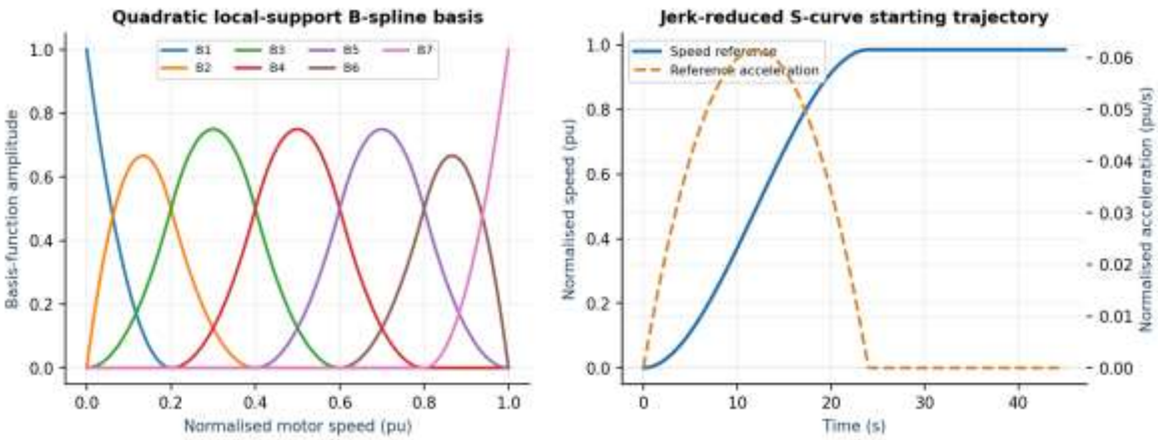

4.4 Sliding-mode-inspired resistance selection

$T^* = \hat{T}L, nom + J_{pu}\frac{d\omega_{ref}}{dt} + kpe + \hat{d} + ks\ \tanh(S/\delta)$ (20)

$X^* = \arg\min_x\{[\mathrm{T}_e(\mathrm{x}) - T^*]^2 + \rho\mathrm{I}[\max(\mathrm{I}_s(\mathrm{x}) - \mathrm{I}_{lim}, 0)]^2 + \rho\mathrm{x}(\mathrm{x} - \mathrm{x}_{old})^2\}$ (21)

The desired torque combines nominal load feedforward, reference acceleration, proportional tracking correction, the learned uncertainty and a bounded sliding-mode-inspired term. A 161-point position search then selects a physically available electrode position while penalising current-limit violation and unnecessary actuator travel. The robust term uses ks = 0.16 and boundary thickness δ = 0.045; the current penalty is 28.0 and the movement penalty is 0.022.

The use of tanh(S/δ) deliberately avoids demanding instantaneous discontinuous movement from a slow mechanical electrode drive. The implementation is therefore accurately described as a bounded sliding-mode-inspired supervisory controller. It should not be interpreted as an experimentally verified ideal sliding-mode switching law or as proof of global stability for the full unmodelled industrial plant.

4.5 Bypass, interlocks and abnormal operating states

The rotor short-circuit contactor is permitted only when the model speed exceeds 0.975 pu and the external resistance falls below 0.012 pu. In a practical implementation, the bypass decision additionally requires verified contactor readiness, healthy position and temperature signals, acceptable rotor current, correct electrode travel and all plant permissives. Independent trip functions must remain effective if the neural estimator freezes, a sensor fails or communications are lost. ABB identifies dedicated contactor applications for short-circuiting motor-starting resistances [14], while IEEE 3004.8 provides the relevant motor-protection context [4].

5. Numerical Methodology and Reproducibility

5.1 Study classification and software environment

This study is an original deterministic, reduced-order numerical simulation implemented in Python using NumPy 2.3.5 and SciPy 1.17.0. It is not a MATLAB/Simulink execution, hardware-in-the-loop test, laboratory prototype, operating-plant measurement or independently certified manufacturer model. MathWorks wound-rotor documentation is cited to establish a possible higher-fidelity future implementation pathway and to clarify rotor-parameter referral; citing that documentation does not imply that the present results were generated with MathWorks software [12, 13, 15].

The model is integrated at a fixed 0.02 s time step over 58 s. Performance indices are accumulated over the first 45 s using trapezoidal numerical integration; root-mean-square error uses the sampled points in the same interval. Every controller is exposed to the same motor parameters, plant disturbance, initial electrode position and ambient conditions within its scenario.

Figure 4. Original deterministic simulation workflow linking the motor, time-varying load, neural estimator, electrode limits and reported performance metrics.

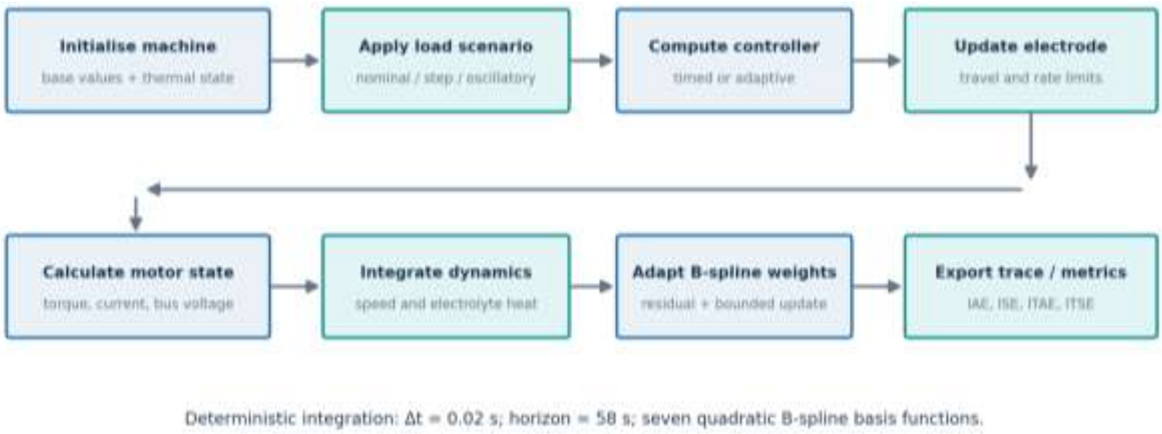

Table 1. Motor, network and base quantities used in every simulation

Parameter	Assigned value	Unit
Rated mechanical output	5.0	MW
Stator line-to-line voltage	6.6	kV
Supply frequency / number of poles	50 / 4	Hz / poles
Synchronous / rated speed	1500 / 1470	rpm
Efficiency / power factor assumptions	0.95 / 0.89	pu / pu
Calculated rated line current	517.3	A
Calculated rated torque	32480.6	N·m
Combined motor/load inertia	3100	kg·m²
Rotor resistance / equivalent leakage reactance	0.025 / 0.22	pu / pu

Parameter	Assigned value	Unit
Magnetising-current approximation	0.28	pu
Torque / current model coefficients	1.20 / 0.72	dimensionless
Network voltage-sensitivity coefficient	0.072	pu V / pu I

Table 2. Liquid starter, thermal model and controller settings

Parameter	Assigned value	Unit
Maximum / minimum geometric LRS resistance	0.360 / 0.008	pu
Reference electrolyte temperature	25	°C
Conductivity temperature coefficient	0.018	$°C^{-1}$
Effective thermal capacity	3.6	MJ/°C
Effective cooling time constant	750	s
Maximum normalised electrode velocity	0.058	s^{-1}
Actuator response time constant	0.28	s
Conventional electrode ramp	39	s
Adaptive S-curve reference duration	24	s
Adaptive current constraint	2.30	pu
Rotor-bypass speed / resistance threshold	0.975 / 0.012	pu / pu
B-spline degree / basis count	2 / 7	degree / functions
Learning rate / leakage	0.24 / 0.035	model units
Tracking gain / sliding gain / boundary	2.00 / 0.16 / 0.045	model units
Integration step / full simulation horizon	0.02 / 58	s / s
Performance-index evaluation window	0–45	s

5.2 Compared controllers and scenario definitions

The conventional controller uses a fixed 39 s linear electrode-position command, subject to the same actuator lag, rate limits and bypass conditions as the adaptive controller. It receives no speed-error correction and no conductivity compensation. The adaptive controller uses the architecture in Section 4 with the same physical actuator and initial state. The conventional ramp is deliberately held constant across all operating cases; it represents a timer-based commissioning setup, not an optimally retuned baseline for every scenario.

Table 3. Operating scenarios and explicitly imposed uncertainty

Scenario	Conductivity κc	Ambient	Applied conditions
A — nominal	1.00	35 °C	Nominal quadratic process load
B — changing load	0.92	38 °C	+0.18 pu step near 14 s; −0.12 pu near 31 s
C — combined stress	0.70	43 °C	8% higher base load, steps and 0.65/1.35 Hz oscillations
Conductivity sensitivity	0.62–1.12	40 °C	Eight operating points with identical disturbed-load law

The nominal load model is $T_{L,pu} = m(0.18 + 0.76\omega_{r,pu}^2)$. In the changing-load and combined-stress cases, smooth logistic changes add approximately 0.18 pu at 14 s and remove 0.12 pu at 31 s. The combined case superimposes sinusoidal torque terms of amplitudes 0.075 and 0.040 pu at 0.65 and 1.35 Hz, with a smooth 12–37 s envelope.

5.3 Performance metrics and units

$$IAE = \int_0^T |e(t)|\,dt, \quad ISE = \int_0^T e^2(t)\,dt \tag{22}$$

$$ITAE = \int_0^T t|e(t)|\,dt, \quad ITSE = \int_0^T te^2(t)\,dt \tag{23}$$

$$RMSE = \sqrt{[(1/N)\sum_{k=1}^{N} e_k^2]} \tag{24}$$

Because speed error is represented in per unit, IAE has units pu·s, ISE has units pu²·s, ITAE has units pu·s², ITSE has units pu²·s² and RMSE has units pu. Each label is used consistently throughout the text and tables. Additional engineering outputs include peak stator current, minimum estimated bus voltage, peak torque, time to 0.95 pu speed, bulk electrolyte temperature rise and integrated LRS energy.

6. Numerical Results

6.1 Scenario A: nominal motor starting

Under healthy electrolyte conductivity and nominal process loading, both controllers complete the start. The adaptive algorithm reduces IAE from 6.721 to 6.003 pu·s (10.7%) and reduces ISE from 2.429 to 2.070 pu²·s (14.8%). The time to reach 0.95 pu speed falls from 30.02 to 27.74 s. The calculated peak stator currents are 1.729 and 1.730 pu, respectively; the approximately 0.002 pu difference is not a practically meaningful peak-current improvement.

Figure 5. Scenario A: independently generated speed, current, electromagnetic torque and effective LRS resistance for conventional and adaptive starting.

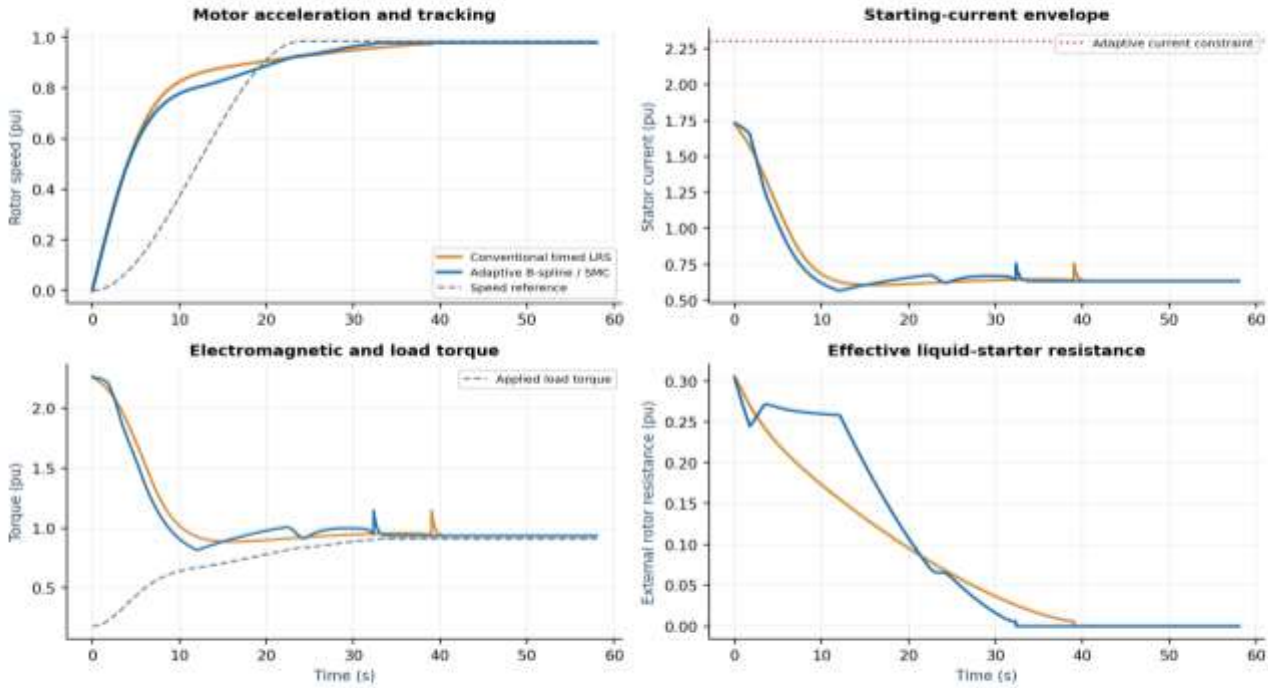

Table 4. Scenario A results: nominal load and healthy electrolyte

Performance quantity	Unit	Conventional	Adaptive
IAE	pu·s	6.721	6.003
ISE	pu²·s	2.429	2.070
ITAE	pu·s²	70.401	58.448
ITSE	pu²·s²	19.871	15.942
RMSE	pu	0.232	0.214
Time to 0.95 pu speed	s	30.020	27.740
Peak stator current	pu	1.729	1.730
Minimum motor-bus voltage	pu	0.948	0.947
Peak electromagnetic torque	pu	2.260	2.261
Electrolyte temperature rise	°C	13.188	13.581
LRS dissipated energy	MJ	49.436	50.504

The starter-energy estimate rises modestly from 49.44 to 50.50 MJ, and the estimated bulk temperature rise increases from 13.19 to 13.58 °C. The adaptive benefit under nominal conditions is therefore more accurate trajectory regulation and a quicker transition to near-rated speed, not simultaneously lower energy, current and temperature.

6.2 Scenario B: changing process load and conductivity drift

When the load changes during acceleration and relative conductivity is reduced to 0.92, the fixed electrode schedule cannot adjust its resistance trajectory in response to the process torque. The adaptive estimator changes the effective torque request as the residual load becomes apparent. IAE decreases from 6.784 to 6.038 pu·s (11.0%), and ITAE decreases from 75.067 to 62.802 pu·s² (16.3%). Time to 0.95 pu improves by 3.20 s.

Figure 6. Scenario B: independently generated response under a process-load increase, subsequent partial unloading and mild conductivity reduction.

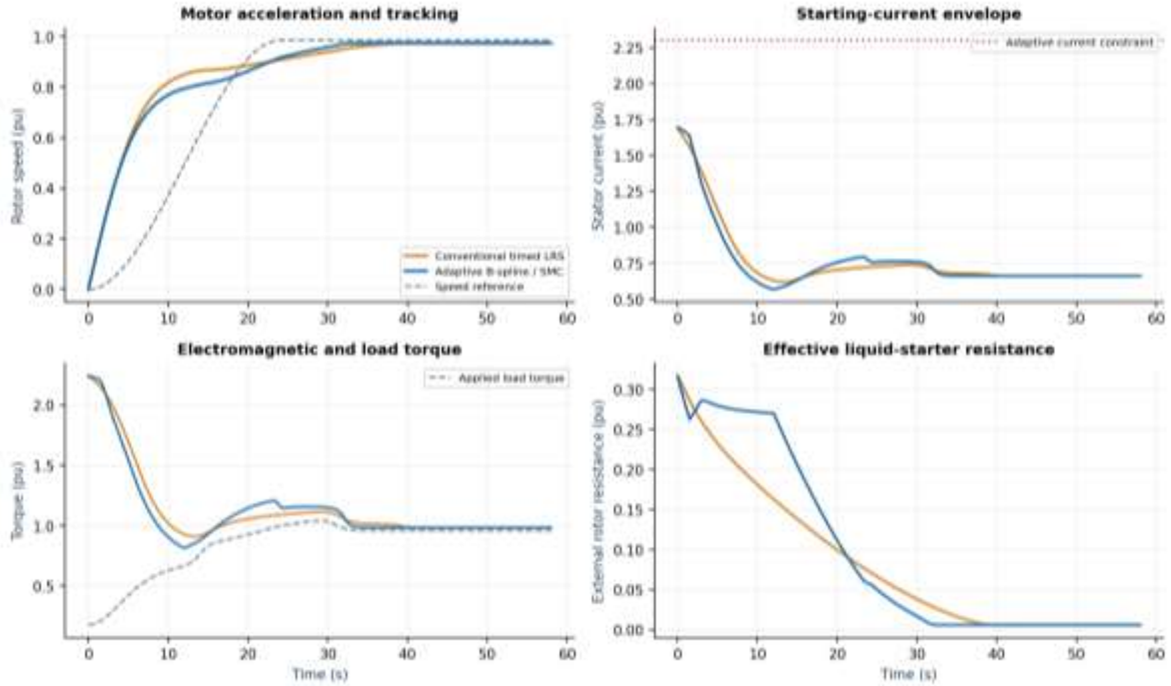

Table 5. Scenario B results: varying process load and mild electrolyte drift

Performance quantity	Unit	Conventional	Adaptive
IAE	pu·s	6.784	6.038
ISE	pu²·s	2.353	1.982
ITAE	pu·s²	75.067	62.802
ITSE	pu²·s²	19.494	15.419
RMSE	pu	0.229	0.210
Time to 0.95 pu speed	s	31.860	28.660
Peak stator current	pu	1.693	1.694

Performance quantity	Unit	Conventional	Adaptive
Minimum motor-bus voltage	pu	0.950	0.950
Peak electromagnetic torque	pu	2.240	2.241
Electrolyte temperature rise	°C	13.825	14.178
LRS dissipated energy	MJ	52.278	53.352

The peak current remains practically the same because both controllers begin with the same physical electrode position and see the same first-instant motor condition. This illustrates a limitation of supervisory adaptation: a controller cannot retroactively remove the instantaneous current associated with an identical initial resistance and an actuator with finite movement speed.

6.3 Scenario C: degraded electrolyte and oscillatory disturbance

The combined-stress case imposes 30% lower conductivity, 43 °C ambient temperature, an 8% higher base load, changing load steps and two oscillatory disturbance components. The adaptive algorithm reduces IAE by 13.2%, ISE by 20.7%, ITAE by 17.3% and ITSE by 25.7%. RMSE decreases from 0.206 to 0.184 pu. The time to 0.95 pu decreases from 33.46 to 30.70 s, corresponding to an 8.2% acceleration-time improvement.

Figure 7. Scenario C: independently generated combined-stress response with conductivity degradation, elevated temperature and multiple-frequency load disturbance.

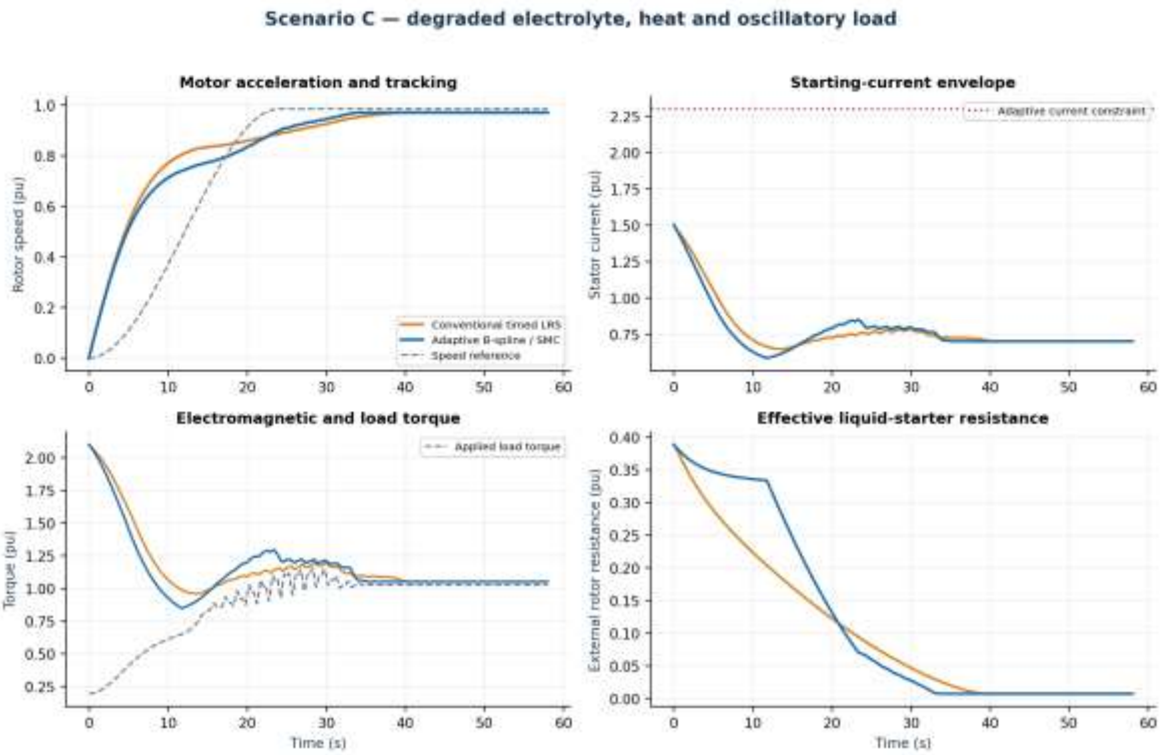

Table 6. Scenario C results: combined conductivity, thermal and load disturbances

Performance quantity	Unit	Conventional	Adaptive
IAE	pu·s	6.398	5.553
ISE	$pu^2·s$	1.913	1.517
ITAE	$pu·s^2$	76.823	63.541
ITSE	$pu^2·s^2$	16.440	12.211
RMSE	pu	0.206	0.184
Time to 0.95 pu speed	s	33.460	30.700
Peak stator current	pu	1.501	1.501
Minimum motor-bus voltage	pu	0.964	0.964
Peak electromagnetic torque	pu	2.102	2.102
Electrolyte temperature rise	°C	15.034	15.352
LRS dissipated energy	MJ	56.979	57.978

Both methods produce the same modelled peak current of 1.501 pu (776.7 A) and the same minimum bus voltage of 0.964 pu. These equal maxima arise from the shared initial condition and must not be misrepresented as evidence that the adaptive controller lowers inrush current. The proposed controller improves trajectory and starting-time objectives under this parameter set, but its starting-current advantage is not demonstrated.

6.4 Bus-voltage and electrolyte-heating trade-off

Figure 8. Scenario C: original estimated motor-bus voltage and lumped bulk-electrolyte temperature for both controllers.

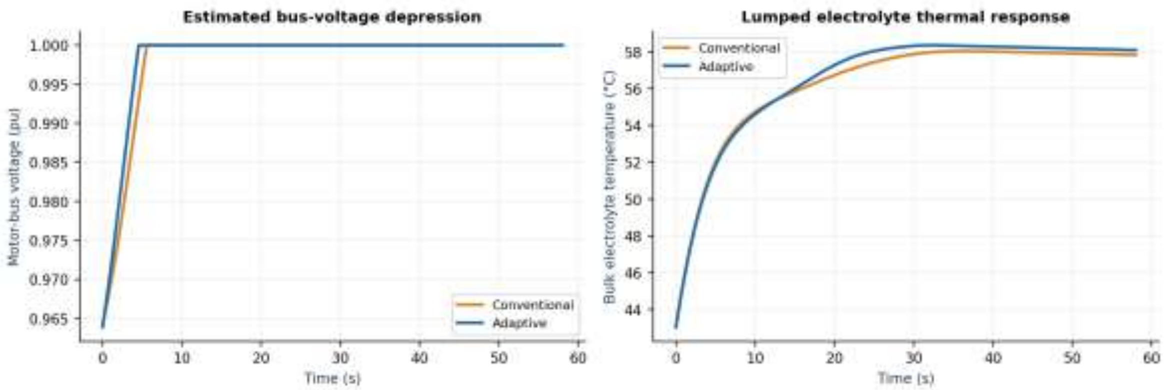

Figure 8 shows that the minimum scalar bus-voltage prediction is essentially unchanged between controllers. More importantly, calculated LRS dissipated energy increases from 56.98 to 57.98 MJ (1.8%), and predicted electrolyte temperature rise increases from 15.03 to 15.35 °C. The increase results from the alternate resistance/speed trajectory chosen to improve tracking. Therefore, accelerated or more accurate starting should be paired with an explicit thermal constraint rather than assumed to guarantee lower starter losses.

6.5 Consistent performance-index comparison

Figure 9. Scenario C performance indices, with the conventional result normalised to 100% and all adaptive values calculated from the present simulation.

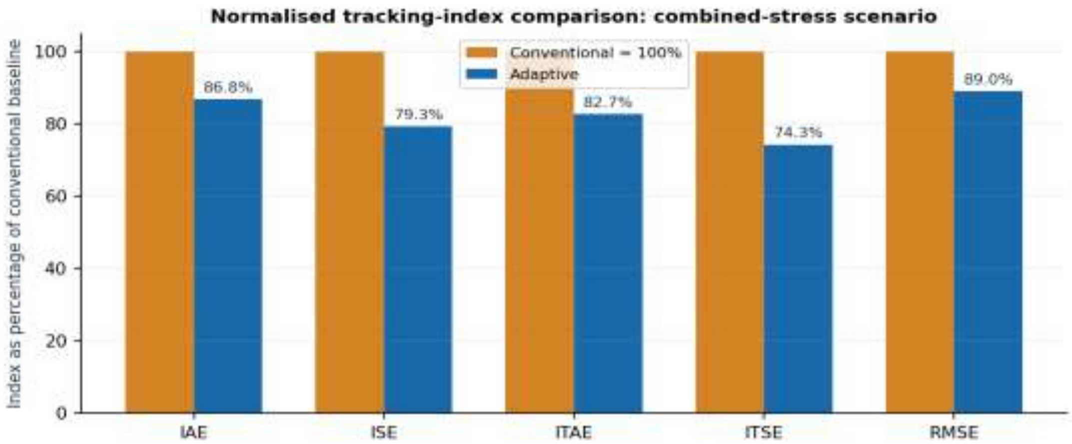

The normalised chart demonstrates consistent reductions across all five speed-tracking indices: IAE 13.2%, ISE 20.7%, ITAE 17.3%, ITSE 25.7% and RMSE 11.0%. The percentage reduction is calculated as 100(C − A)/C, where C and A are the conventional and adaptive values for the same metric and scenario. No values are taken from earlier neural-control publications.

6.6 Sensitivity to electrolyte conductivity

Figure 10. Original eight-point conductivity sensitivity sweep showing tracking-error and peak-current behaviour under the same disturbed-load law.

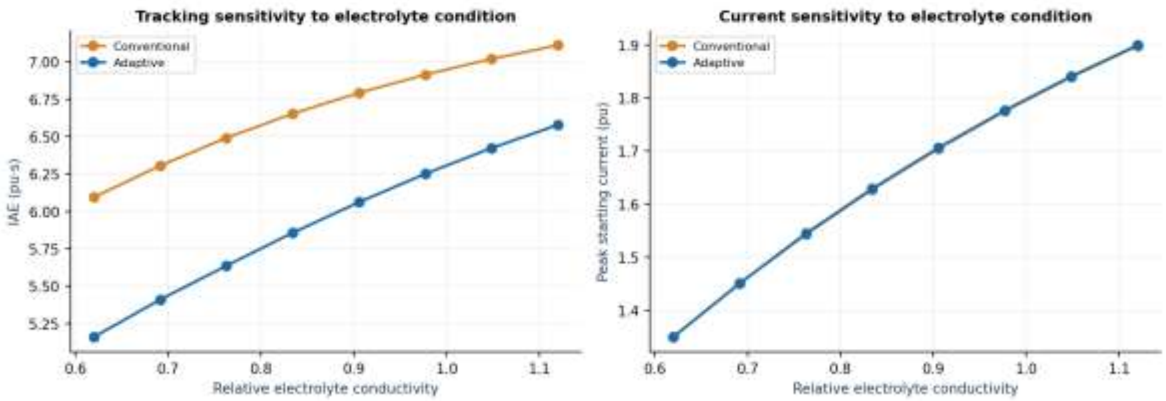

An eight-point sweep varies relative conductivity from 0.62 to 1.12 while holding the disturbance law and model structure constant. At the lowest conductivity, IAE changes from 6.094 to 5.159 pu·s; at the highest conductivity it changes from 7.111 to 6.579 pu·s. The adaptive architecture lowers IAE across all evaluated points, while its peak-current curve is nearly coincident with the conventional curve. The sweep therefore supports robustness of the tracking improvement within the investigated parameter range, but it does not establish a universal current-reduction benefit.

7. Discussion and Industrial Implementation

7.1 Meaning of the observed performance improvements

The principal contribution is the linkage of online uncertainty estimation to the actual manipulated quantity available in a conventional liquid starter: electrode position. Unlike a general inverter-fed motor-control claim, the proposed algorithm respects a bounded, relatively slow mechanical actuator and allows conductivity and electrolyte heating to influence the effective resistance. The resulting reduction in IAE, ISE, ITAE and ITSE reflects improved agreement with a chosen speed reference, while faster attainment of 0.95 pu provides a directly interpretable starting-time benefit.

These outcomes should not be conflated with a validated reduction in peak inrush, mechanical fatigue, equipment lifetime or total process energy. Peak current is almost identical in the reported cases; the simplified torque-ripple statistic can be higher for the adaptive controller because active resistance adjustments respond to the imposed disturbance; and the integrated liquid-starter loss increases slightly. A scientifically defensible interpretation must report these trade-offs rather than selectively highlighting only the favourable tracking indices.

7.2 Measurement, instrumentation and embedded implementation

A practical retrofit requires measured stator current, motor-bus voltage, shaft speed, electrode position, bulk electrolyte temperature and a reliable starter-ready/permissive state. Optional conductivity measurement can improve feedforward correction, while rotor current and tank level improve diagnostics. A PLC or industrial embedded controller should execute the supervisory calculation at a rate compatible with electrode mechanics, using watchdog supervision, sensor-range checks and a deterministic return to a validated fixed-ramp mode when adaptive operation becomes unavailable.

Because the quadratic network contains only seven locally supported basis functions, the estimator is computationally modest. The demonstrated grid search uses 161 candidate positions; an industrial implementation could reduce the search resolution, use a precomputed torque/resistance map or solve a bounded one-dimensional optimisation. Any control software must be documented, version managed, validated against motor protection coordination and tested for power restoration, actuator stall, communication loss and contactor disagreement.

7.3 Protection, hazardous areas and standards applicability

The applicable general rotating-machine rating and performance reference is IEC 60034-1:2026 [16]. Hazardous-area electrical design, equipment selection, installation and initial inspection must be addressed under IEC 60079-14:2024 where the installation is in or associated with an explosive atmosphere; inspection and maintenance obligations are described by IEC 60079-17:2023 [11, 17]. Motor protection should remain coordinated with IEEE 3004.8, while plant starting and network-voltage assessment require a proper IEEE 3002.7 study [3, 4].

Standards must not be misapplied. IEC 60034-12:2024 concerns starting performance of specified single-speed three-phase cage motors at rated voltages up to 1,000 V and is not directly a 6.6 kV wound-rotor/LRS standard [18]. Likewise, API 541 and API 547 primarily address designated squirrel-cage motor categories rather than establishing direct compliance requirements for the wound-rotor starter studied here. Petroleum-industry procurement expectations can inform data-sheet completeness, but actual applicability must be determined from project specifications and the motor construction [19].

7.4 Practical thermal optimisation

The present controller penalises current-limit violation and electrode travel, but it does not explicitly penalise accumulated LRS heat. This design choice explains why tracking and acceleration can improve while starter energy increases. A suitable extension is to augment the optimisation cost with a temperature-dependent weight, a predicted remaining-start energy term and a hard maximum-electrolyte-temperature constraint. Such an extension would expose the true multiobjective nature of motor starting: current, voltage sag, acceleration time, rotor losses, mechanical torque and starter temperature cannot all be minimised independently.

For installations involving repeated starts, the cooling interval and initial electrolyte temperature are especially important. Bulk-temperature measurement alone may be inadequate where electrode heating is strongly localised. Tank mixing, electrolyte level, contamination, ventilation, compatible materials and manufacturer's limits must be incorporated before the controller is considered suitable for field commissioning.

8. Limitations and Verification Path

- The model is a deterministic reduced-order screening model. It does not resolve stator/rotor flux-linkage dynamics, detailed d–q transients, magnetic saturation, detailed harmonic content or the electrical angle of the source impedance.
- Motor equivalent-circuit constants, actuator settings and thermal parameters are assumed engineering-study values, not identified from a specific 5 MW machine or a particular manufacturer's certified liquid starter.
- The conductivity law is a first-order approximation. Real sodium-carbonate or other approved electrolyte behaviour can depend nonlinearly on concentration, temperature, contamination and electrode geometry; the actual chemical specification must follow the starter manufacturer's instructions.
- No laboratory measurements, site commissioning traces, prototype tests, hardware-in-the-loop results or independent statistical repetitions are claimed. The comparisons are deterministic numerical cases, not experimentally established improvements.
- The conventional baseline is a fixed 39 s timed ramp; a retuned PI, model-predictive or optimally scheduled LRS baseline could narrow the reported advantage.
- The reported peak-current and voltage-sag figures are model estimates, not relay records or measured feeder waveforms. No equipment-life or quantified mechanical-fatigue improvement is established.
- The stability reasoning is local and implementation-oriented. A complete Lyapunov proof for the coupled actuator, thermal state, bypass switching and parameter uncertainty remains future work.

The recommended verification sequence is: identify the actual wound-rotor equivalent circuit and torque/speed curve; characterise LRS resistance against electrode travel, temperature and conductivity; validate the plant-source model using a formal motor-starting study; implement the controller first in a higher-fidelity wound-rotor environment; perform hardware-in-the-loop and instrumented low-power trials; and proceed to an approved industrial pilot only after independent protection and hazardous-area review. IEC 60034-2-1 and IEC 60034-2-2 provide relevant contexts for machine-loss and efficiency testing, but the specific starter validation procedure must be project- and manufacturer-approved [20, 21].

9. Conclusion

This paper has presented a physically consistent, AI-assisted supervisory control architecture for a liquid resistance starter connected to a high-power wound-rotor induction motor. The method combines a smooth speed reference, a seven-function quadratic B-spline uncertainty estimator, a bounded sliding-mode-inspired correction and constrained electrode-position selection. It explicitly represents conductivity, bulk electrolyte temperature, actuator travel limits and rotor bypass sequencing.

In an independently generated reduced-order numerical study of a 5 MW, 6.6 kV motor, the most demanding combined-stress case produced reductions of 13.2% in IAE, 20.7% in ISE, 17.3% in ITAE and 25.7% in ITSE. Time to 95% synchronous speed decreased from 33.46 to 30.70 s. However, peak current and minimum estimated bus voltage were effectively unchanged, while LRS energy increased by approximately 1.8%.

The defensible conclusion is therefore that adaptive resistance positioning can improve the selected trajectory-tracking and acceleration objectives within the assumptions of the model, but it does not automatically reduce inrush current or starter heat. Future work should prioritise manufacturer-specific parameter identification, explicit thermal constraints, stronger conventional-controller baselines, high-fidelity wound-rotor simulation, laboratory experiments and controlled industrial field validation.

Acknowledgements

The authors acknowledge their professional affiliation with the Technical and Administrative Training Institute (TATI), Muscat, Oman. No institutional sponsorship, provision of industrial test facilities or organisational endorsement is implied unless separately authorised by the institution.

References

1. AOIP, "EPM: Electrolytic starter (LRS) for high-power slipring motors," manufacturer technical documentation. Available: https://www.aoip.com/product/electrolytic-starters-for-slipring-motors/epm/ (accessed 18 Aug. 2026).
2. AOIP, "Electrolytic starters for slipring motors," manufacturer product overview. Available: https://www.aoip.com/cat/electrolytic-starters-for-slipring-motors/ (accessed 18 Aug. 2026).
3. IEEE Standards Association, IEEE 3002.7-2018, IEEE Recommended Practice for Conducting Motor-Starting Studies and Analysis of Industrial and Commercial Power Systems. Available: https://standards.ieee.org/ieee/3002.7/4435/
4. IEEE Standards Association, IEEE 3004.8-2016, IEEE Recommended Practice for Motor Protection in Industrial and Commercial Power Systems. Available: https://standards.ieee.org/ieee/3004.8/5028/
5. F. Beltran-Carbajal, H. Yanez-Badillo, D. Galvan-Perez, I. Rivas-Cambero, D. Sotelo and C. Sotelo, "B-Spline Artificial Neural Networks in Robust Induction Motor Control," IEEE Access, vol. 12, pp. 101679–101700, 2024, doi: 10.1109/ACCESS.2024.3430323.
6. R. Tapia-Olvera, A. Valderrabano-Gonzalez and F. Beltran-Carbajal, "Efficient Adaptive Regulation Strategy for Control Position of Induction Motors," IEEE Access, vol. 12, pp. 38512–38524, 2024, doi: 10.1109/ACCESS.2024.3375346.
7. ABB, "Engineering efficiency in mining: Enhancing safety, reliability and productivity," industrial motor application brochure. Available: https://library.e.abb.com/public/62596a35cd344e71bdbf6b469cfd5052/Mining_brochure_3AXD50000529377_REV%20A_EN.pdf
8. N. M. Patrikalakis, T. Maekawa and W. Cho, "1.4.2 B-spline curve," Massachusetts Institute of Technology hyperbook. Available: https://web.mit.edu/hyperbook/Patrikalakis-Maekawa-Cho/node17.html

9. V. I. Utkin, Sliding Modes in Control and Optimization. Berlin: Springer, 1992, doi: 10.1007/978-3-642-84379-2.
10. V. I. Utkin, "Sliding Modes in Control of Electric Motors," in Sliding Modes in Control and Optimization, Springer, 1992, pp. 250–264, doi: 10.1007/978-3-642-84379-2_17.
11. International Electrotechnical Commission, IEC 60079-14:2024, Explosive atmospheres—Part 14: Electrical installation design, selection and installation of equipment, including initial inspection. Available: https://webstore.iec.ch/en/publication/66049
12. MathWorks, "Induction Machine Wound Rotor," Simscape Electrical documentation. Available: https://www.mathworks.com/help/sps/ref/inductionmachinewoundrotor.html (accessed 18 Aug. 2026).
13. MathWorks, "FEM-Parameterized Induction Machine (Wound Rotor)," Simscape Electrical documentation. Available: https://www.mathworks.com/help/sps/ref/femparameterizedinductionmachinewoundrotor.html (accessed 18 Aug. 2026).
14. ABB, "R contactors: Control of AC and DC power circuits," contactor technical catalogue, 2015. Available: https://library.e.abb.com/public/c89347ab617a4dc4801b9529978dc2b2/1SXU106047C0201_RContactorsCatalogJuly2015.pdf
15. MathWorks, "Induction Machine Measurement," Simscape Electrical documentation. Available: https://www.mathworks.com/help/sps/ref/inductionmachinemeasurement.html (accessed 18 Aug. 2026).
16. International Electrotechnical Commission, IEC 60034-1:2026, Rotating electrical machines—Part 1: Rating and performance. Available: https://webstore.iec.ch/en/publication/89961
17. International Electrotechnical Commission, IEC 60079-17:2023, Explosive atmospheres—Part 17: Electrical installations inspection and maintenance. Available: https://webstore.iec.ch/en/publication/64810
18. International Electrotechnical Commission, IEC 60034-12:2024, Rotating electrical machines—Part 12: Starting performance of single-speed three-phase cage induction motors. Available: https://webstore.iec.ch/en/publication/78133
19. American Petroleum Institute, "API Standard 541: Form-Wound Squirrel Cage Induction Motors—375 kW (500 Horsepower) and Larger," product announcement and scope, 2014. Available: https://www.api.org/~/media/files/publications/whats%20new/541_e5%20pa.pdf
20. International Electrotechnical Commission, IEC 60034-2-1:2024, Rotating electrical machines—Part 2-1: Standard methods for determining losses and efficiency from tests. Available: https://webstore.iec.ch/en/publication/67756
21. International Electrotechnical Commission, IEC 60034-2-2:2024, Rotating electrical machines—Part 2-2: Specific methods for determining separate losses of large machines from tests. Available: https://webstore.iec.ch/en/publication/67757